Supplemental Information

Structural basis for the regulation of the SCF cycle by CSN and ubiquitination substrates

Radoslav I. Enchev, Daniel C. Scott, Paula C. A. da Fonseca, Anne Schreiber, Julie K. Monda, Brenda A. Schulman*, Matthias Peter* and Edward P. Morris*

Supplemental Figures

Figure S1. Single particle electron microscopy analysis of CSN-SCF complexes. (**A-C, E-F**) Electron microscopy and single particle analysis of the (**A**) $CSN^{Csn5H138A}$-SCF~$N8^{Skp2/Cks1}$, (**B**) $CSN^{Csn5H138A}$, (**C**) $CSN^{Csn5H138A}$-SCF~$N8^{Fbw7}$, (**E**) $CSN^{\Delta Csn5}$-SCF~$N8^{Skp2/Cks1}$, and (**F**) $CSN^{Csn2\Delta N1-269}$ datasets. Characteristic electron micrographs in negative stain are shown in the top panel. Circles indicate examples of molecular images. The middle panels show a representative selection of refined class averages (top), re-projections of the 3D structure (middle) and corresponding surface views (bottom row). Fourier Shell Correlation based resolution estimates are shown in the bottom panels. (**D**) Coomassie-stained SDS-PAGE of the recombinant $CSN^{\Delta Csn5}$ and $CSN^{Csn2\Delta N1-269}$ as well as the *in vitro* reconstituted $CSN^{\Delta Csn5}$-SCF~$N8^{Skp2/Cks1}$ complex after size exclusion chromatography. Related to Figure 1.

Figure S2. Supporting data for the CSN molecular model (**A**) Orthogonal surface views of the CSN segment from the $CSN^{Csn5H138A}$-SCF~$N8^{Skp2/Cks1}$ map (top) and the 26S proteasome Lid (bottom) from (da Fonseca et al., 2012), shown in similar orientations. (**B**) Atomic models for CSN subunits generated by the I-Tasser structural prediction server (Roy et al., 2010) and corresponding diagrams of the domain distribution. (**C**) Atomic models for the N-terminally truncated Csn2 constructs. The N-terminus of Csn2 was predicted to comprise a capping N-terminal α-helix, followed by six helical-repeat motifs. Note the similarity to the N-terminus of the recently solved structure of the Csn2 paralogue Rpn6, which also contains a capping N-terminal helix, followed by five TPR-like helical repeats (Pathare et al., 2012). The three truncation constructs used in this study are thus predicted to be lacking the capping helix and two ($CSN^{Csn2\Delta N1-104}$), four ($CSN^{Csn2\Delta N1-185}$) or six ($CSN^{Csn2\Delta N1-269}$) TPR-like motifs. (**D**) Quantitative evaluation of the fit of the atomic models for the indicated subunits in the $CSN^{Csn5H138A}$-SCF~$N8^{Skp2/Cks1}$ map. Correlation coefficients were calculated within local masks over the resolution range 400 – 25 Å using the program Uro (Navaza et al., 2002). The correlation coefficients for the smallest subunits, Csn7 and Csn8, as well as Skp1 and Cks1 are anomalously high due to their globular shape and the limited resolution of the current analysis. Related to Figure 2.

Figure S3. Difference map analysis and Nedd8 docking (**A**) Structural comparison (left) and difference map analysis (middle and right) between (left hand side) $CSN^{Csn5H138A}$-SCF~$N8^{Skp2/Cks1}$ (cyan mesh) and $CSN^{Csn5H138A}$ (grey surface) to locate the CSN segment in the $CSN^{Csn5H138A}$-SCF~$N8^{Skp2/Cks1}$ map;

and (right hand side) of $CSN^{Csn5H138A}$-SCF~$N8^{Fbw7}$ (purple mesh) and $CSN^{Csn5H138A}$ (grey surface) to locate the CSN segment in the $CSN^{Csn5H138A}$-SCF~$N8^{Fbw7}$ map. Within the difference maps the segments corresponding to the SCF~$N8S^{kp2/Cks1}$ and SCF~$N8^{Fbw7}$ are color-coded in cyan and purple; difference densities within the regions interpreted as Csn1, Csn3 and Csn4 (see Figure 2) are shown in grey, green and yellow respectively. Interestingly, Csn1 and Csn3 and perhaps also Csn4 are involved in SCF binding (see Discussion and (Gusmaroli et al., 2007)). (**B**) Structural comparison (left) and difference map analysis (middle and right) between (left hand side) $CSN^{Csn5H138A}$-SCF~$N8^{Skp2/Cks1}$ (cyan mesh) and $CSN^{\Delta Csn5}$-SCF~$N8^{Skp2/Cks1}$ (pink surface) to locate Csn5 (cyan surface); and (right hand side) $CSN^{Csn5H138A}$ (grey mesh), and $CSN^{Csn2\Delta N1\text{-}269}$ (yellow surface) to locate the $Csn^{N1\text{-}269}$ segment (orange surface). (**C**) Segmented surface views of the $CSN^{Csn5H138A}$-SCF~$N8^{Skp2/Cks1}$ map showing the SCF~$N8^{Skp2/Cks1}$ density segment in grey, the CSN in yellow and the Csn2 and Csn5 regions in pink and blue respectively. (**D-F**) Tentative docking of Rbx1, $Cul1^{691\text{-}776}$ and Nedd8 into the SCF~$N8^{Skp2/Cks1}$ segment of the $CSN^{Csn5H138A}$-SCF~$N8^{Skp2/Cks1}$ map. (**D**) The density attributed to CSN is shown as an orange surface, the $SCF^{Skp2/Cks1}$~N8 density is rendered as a gray mesh and the atomic coordinates of individual subunits are color-coded as in (**E**). After docking the atomic coordinates for $Cul1^{1\text{-}690}$-Skp1-Skp2-Cks1, a segment attributed to $SCF^{Skp2/Cks1}$~N8 located between Csn5, Csn4 and Csn2 is still left empty (red circle). (**E**) Rbx1 and $Cul1^{691\text{-}776}$-Nedd8 (WHB~N8) can be docked into this segment. The Rbx1 conformation chosen here is as in the non-neddylated Cul1/Rbx1/Skp1/Skp2 model (Zheng et al., 2002) but see also Figure 6A. The position of WHB-N8 was adjusted by rotating helix29, which is known to allow a flexible orientation of the WHB subdomain in neddylated cullins (Duda et al., 2008). (**F**) The whole $CSN^{Csn5H138A}$-SCF~$N8^{Skp2/Cks1}$ map is shown as a grey mesh with docked atomic models for all CSN subunits. A dashed circle shows the region where Nedd8 is positioned closely to the active site of Csn5. In this orientation Rbx1 is positioned close to Csn2 and Csn4. Related to Figures 1 and 3.

Figure S4. Biochemical characterization of CSN and SCF complexes. (**A-E)** Individual complexes (identified on the left of each blot – neddylated complexes are marked ~N8) were analyzed by analytical size exclusion chromatography as described for Figure 4. The fractions in which particular complexes were eluted are identified above each blot. (**F**) Coomassie-stained SDS-PAGE of the CSN complexes used in this study and overlay of the corresponding Superose6 size exclusion chromatography profiles. Note that the display of the chromatography profiles (elution volume) is off-set by one fraction. (**G**) Deneddylation assays of $Cul1^{CTD}$~N8/Rbx1 with each of the CSN constructs used in this study; neddylated (~N8, upper band) and un-neddylated (lower band) $Cul1^{CTD}$ was visualized by imunnoblotting with anti-Cul1 antibodies. (**H-K**) Immunoblot analysis of Superose6 elutions of $CSN^{Csn2\Delta N1\text{-}185}$ with Cul1~N8/Rbx1, (**H**), and $CSN^{Csn2\Delta N1\text{-}104}$ with $SCF^{Skp2/Cks1}$, (**I**), and CAND1-$SCF^{Skp2/Cks1}$ and CSN-CAND1-$SCF^{Skp2/Cks1}$ complexes (**K**). The labeling scheme is as described in A-E. Related to Figure 4.

Figure S5. Control analytical size exclusion data for the experiments presented in **Figure 5B**. Related to Figure 5.

Figure S6. Reciprocal regulation of CSN and SCF. (**A**) The deneddylation of full-length ($Cul1^{FL}$), split-and-co-expressed Cul1 ($Cul1^{SCE}$) and the Cul1 C-terminal domain ($Cul1^{CTD}$) by recombinant CSN was analyzed by immunoblotting with Cul1 antibodies (left panels). Note that in contrast to $Cul1^{FL}$, the two fragments of the $Cul1^{SCE}$ separate upon SDS PAGE analysis, and only the $Cul1^{CTD}$ fragment was probed by immunoblotting. The deneddylation activity of recombinant and endogenous human CSN (purchased from Enzo Life Sciences) were compared, using neddylated $Cul1^{CTD}$ as a substrate (right panel). (**B**) The deneddylation of different $Cul1^{SCE}$~N8/Rbx1 complexes by CSN was monitored by the loss of the $Cul1^{CTD}$~N8 and the appearance of $Cul1^{CTD}$ using immunoblotting, and quantified by plotting normalized $Cul1^{CTD}$ formation as a function of time. (**C**) Poly-ubiquitination of phospho-p27 by SCF~$N8^{Skp2/Cks1}$ in the presence of $CSN^{Csn5H138A}$, $CSN^{\Delta Csn5}$ or $CSN^{Csn2\Delta N1\text{-}269}$. The ubiquitination experiment was performed as described in Figure 6B. (**D**) Poly-ubiquitination of phospho-p27 by $SCF^{Skp2/Cks1}$ complexes assembled with either with neddylated wild type Cul1 (Cul1~N8) or the non-neddylatable Cul1-K720R mutant ($Cul1^{K720R}$) was measured in the presence (+) or absence (-) of $CSN^{Csn5H138A}$. Note that $CSN^{Csn5H138A}$ is able to inhibit ubiquitination activity irrespective of the Cul1 neddylation state (**E**) K48-linked poly-ubiquitin chains, containing a mix of three to seven ubiquitin moieties (BostonBiochem), were incubated in buffer or with indicated concentrations of $CSN^{Csn5H138A}$ or the catalytic domain of the K48-specific de-ubiquitinating enzyme Usp2 (Usp2cc). The reaction conditions replicate the experiment in Figure 6B and S6C. De-conjugation of the poly-ubiquitin chains was monitored as a function of time by immunoblotting with anti-ubiquitin antibodies. (**F**) Two surface views of the $CSN^{Csn5H138A}$-SCF~$N8^{Fbw7}$ map at indicated orientations. Modeling of the location of a $CyclinE^{phospho\text{-}peptide}$ in the $CSN^{Csn5H138A}$-SCF~$N8^{Fbw7}$ complex. CSN is shown as an orange surface, the SCF^{Fbw7}~N8 density is rendered as a gray mesh and the atomic coordinates of individual subunits are color-coded as in Figure 3B. The WD40 repeat of Fbw7 is indicated by a circle and the potential position of the $CyclinE^{phospho\text{-}peptide}$ is marked by an arrow. (**G**) Neddylated (~N8) SCF^{Fbw7} complexes were incubated with equimolar amounts of deneddylation-defective $CSN^{Csn5H138A}$ in the presence (upper panel) or absence (lower panel) of biotinylated $CyclinE^{phospho\text{-}peptide}$ as indicated. The complexes were analyzed by size exclusion chromatography and co-elution of Cul1 and Csn5 was followed by immunoblot analysis as described in Figure 4. Co-elution of the $CyclinE^{phospho\text{-}peptide}$ was analyzed by dot-blot analysis. Related to Figure 6.

Figure S7. (**A**) Pulse-chase [^{32}P]~ubiquitin transfer experiment was performed as described in Figure 3B. The ability of neddylated Cul1-species indicated on the left to stimulate Cdc34's intrinsic ubiquitin transfer ability to lysine-less ubiquitin (Ub_{K0}) was assayed in the presence (+) or absence (-) of cullin and the indicated CSN constructs. (**B**) A zoomed-in surface view of the $CSN^{Csn5H138A}$-SCF~$N8^{Skp2/Cks1}$ map, color-coded as in Figure 6A, showing an overlay of all reported Rbx1 conformations without (left) or with docked Glmn model (right). Cul1 (without Helix29 and WHB) is shown in green, Rbx1 orientations are shown as hues of red, Glmn orientations as hues of blue. The Rbx1-Glmn interaction is based on ((Duda et al., 2012); PDB identifier 4F52). Note that the Glmn coordinates clash with the

electron density assigned to CSN (transparent orange surface) in all orientations, indicating potential steric incompatibility with Glmn binding. Related to Figure 6.

Supplemental Experimental Procedures

Protein expression and purification

CSN expression constructs used in this study were prepared using the MultiBac system, following the strategy described in (Enchev et al., 2010). However, we substituted the C-terminal StrepII-tag on Csn3 for an N-terminal StrepII^{2x}-tag, which significantly increased purification yields. Moreover, only one isoform of Csn7, Csn7b, was included to increase structural homogeneity. Thus, wild type CSN and the active site mutated CSN^{Csn5H138A} constructs were generated from pUCDM-Csn2/^{StrepII2x}3/6/8 and pFBDM-Csn1/4/^{His6}5$^{wt\ or\ H138A}$/7b. For the CSN constructs harboring Csn5 deletion or N-terminal Csn2 truncations we used only pFBDM transfer vectors with the following cassettes: Csn4/7b; Csn1/^{His6}5$^{wt\ or\ H138A\ or\ missing}$; Csn^{StrepII2x}3/2$^{wt\ or\ N\text{-}terminally\ truncated}$; Csn6/8. DNA sequences for all individual proteins were verified as wild type or the desired mutants by sequencing. Restriction digests were used to control correct assembly of the MultiBac transfer vectors.

A single baculovirus for each of the CSN variants was produced, amplified, expressed and purified over a Strep-Tactin Superflow Cartridge (Qiagen) as described in (Enchev et al., 2010). Due to the increased purification yields after the affinity column, the CSN purification protocol was enhanced by the following steps: the StrepII^{2x} tag was usually cleaved at this stage, all fractions were pooled and PreScission protease was added in a 1:50 molar ratio. Cleavage was performed overnight in a dialysis tube in 2 L dialysis buffer (25 mM HEPES, pH 7.5, 150 mM NaCl, 2% glycerol, 2 mM DTT). The pooled Strep-Tactin elution fractions (cleaved or uncleaved) were concentrated to 5 ml with a 50 kDa cut-off concentrator (Amicon) and loaded on a Sephacryl 300 16/60 size exclusion column (GE Healthcare) buffer exchanging into 15 mM HEPES pH 7.5, 200 mM NaCl, 2% glycerol and 2 mM DTT. Fractions from the first Sephacryl 300 peak were pooled and diluted to 50 ml in buffer A (15 mM HEPES pH 7.5, 50 mM NaCl, 2% glycerol, 2 mM DTT). This protein solution was loaded with a 50 ml superloop onto a 6ml ResourceQ anion-exchange column (GE Healthcare) and eluted using a gradient from 50 to 400 mM NaCl over 40 CV with buffer B (15 mM HEPES pH 7.5, 1 M NaCl, 2% glycerol, 2 mM DTT). If

the sample was used for EM analysis, an additional Superose 6 10/300 size exclusion (GE Healthcare) purification step was performed with the peak fraction from the ResourceQ run. Fractions were usually sufficiently concentrated and no additional concentrating step was required. The fraction was loaded with a 500 µl loop, buffer exchanging back to 15 mM HEPES pH 7.8, 150 mM NaCl, 1% glycerol and 1 mM DTT. Typical CSN yields after this step were between 5 and 10 mg from 1 L of High Five cells. The sample was either aliquoted, flash frozen in liquid nitrogen and stored at -80 °C or directly used for EM analysis.

The full-length ^{StrepII2x}Cul1/Rbx1 baculovirus expression construct was generated, expressed and purified as described in (Enchev et al., 2010).

Split-and-coexpress Cul1/Rbx1; split-and-coexpress Cul1$^{\Delta WHB}$/Rbx1; split-and-coexpress Cul1/Rbx1$^{\Delta RING}$; Cul1^{CTD}/Rbx1; Cul1^{WHB}; Cks1; CyclinA; Cdk2; and p27 as well as neddylation and ubiquitination reagents were generated, expressed and purified as described in (Duda et al., 2008). Human Ubc12 was expressed in insect cells and purified on a C-terminal His6-tag. Analogously to its yeast homologue (Scott et al., 2011) Ubc12 was thus purified in an N-terminally acetylated state. Assembly of Skp1/F-box expression constructs was achieved by cloning either full-length Skp2 or Fbw7$^{\Delta N1-263}$ into pGEX4T1-TEV with EcoRI/SalI. Full-length Skp1 was cloned into the NotI/NotI sites of the respective pGEX4T1-TEV Fbw7$^{\Delta N1-263}$ or Skp2$^{full-length}$ vectors. Recombinant baculoviruses were generated by standard procedures and the protein was produced by co-infection of Sf9 insect cells. Skp1/F-box heterodimeric complexes were affinity-purified over gluthatione sepharose beads (GE Healthcare), the GST-tag was cleaved with TEV and Skp1/F-box was further purified over ResourceQ ion exchange and Superdex200 size exclusion chromatography. A common chaperone contaminant, DnaK, was usually removed by supplementing the running buffer with 2 mM ATP and 10 mM $MgCl_2$ before using Skp1/F-box constructs for CSN interaction studies or structural analysis.

Variant CSN-SCF complexes for EM data collection were purified over two steps. First the CSN variant purified over the affinity, ion exchange and size exclusion chromatography steps but with an un-cleaved StrepII^{2x} tag on Csn3 was immobilized on a 1 ml Strep-Tactin Superflow Cartridge with the Superose 6 buffer described above. After washing with 10 CV, the SCF variant with cleaved StrepII^{2x} tag on Cul1 was loaded in two- to three-fold molar excess. Following a wash with 10 CV, the complexes were eluted by supplementing the buffer with 2.5 mM desthiobiotin in 200

µl fractions. Without further concentration the two peak fractions were loaded onto a Superose 6 10/300 size exclusion column and the peak fraction sample was used for electron microscopy.

Antibodies

Antibodies against CSN subunits were purchased as a sampler pack (Enzo LifeSciences, BML-PW8945-0001). Antibodies against Cullin1 were either from Rockland Immunochemicals (C-terminal specific, cat #100-401-A01) or from Santa Cruz Biotechnology (AS97, cat # sc-12761 and H-213, cat # sc-11384); anti-Skp1 from Santa Cruz Biotechnology (N-19, cat # sc-1569); anti-Skp2 from Zymed (cat #51-1900), anti-Fbw7 from AbNova (cat # H00055294-MO2); anti-p27 from Santa Cruz Biotechnology (N-20, cat # sc-527); anti phospho-p27 from Santa Cruz Biotechnology (Thr187, cat # sc-16324); anti-CyclinA from Santa Cruz Biotechnology (H-432, cat # sc-751); anti-Cdk2 from Santa Cruz Biotechnology (G-298, cat # sc-748); anti-CAND1 from Rockland Immunochemicals (N-terminal specific, cat #100-401-A11); anti-ubiquitin from Santa Cruz Biotechnology (P4D1) and anti-His_5 from Qiagen (cat #34698). The anti-Nedd8 antibody was as described in (Souphron et al., 2008).

Secondary antibodies (anti-mouse, anti-rabbit and anti-goat) were HP-conjugated and purchased from GE Healthcare (respectively cat# NA9310, NA934 and PA42002).

Immunoblotting and quantifications

Immunoblots developed with ECL Plus (GE Healthcare) were scanned on a Phosphoimager, whereas immunoblots developed on film were subsequently scanned and quantified using ImageJ (rsbweb.nih.gov/ij/). The signal intensity for the de-neddylated Cul1 band formed at the last time point was set to be 100%, and the signals for all other bands in the gel normalized to that value.

De-ubiquitination assays

In the de-ubiquitination assay (Figure S6E) we used 30 ng/µl of the K48-linked poly-ubiquitin chains (BostonBiochem, uc-220), which corresponds approximately to 1 µM, and 500 nM $CSN^{Csn5H138A}$ or recombinantly produced and purified catalytic domain of Usp2 (a kind gift by S. Kaiser and R. Kopito).

Negative stain electron microscopy

Quantifoil grids (R2/2 Cu 400 mesh) coated with thin carbon floated from mica were glow-discharged for 30 seconds at 50 mA and 0.2 mbar vacuum. 3 µl purified samples were applied for 1 min to the grids. Following two brief buffer washes, the grids were stained with 2% uranyl acetate, gently blotted using filter paper and air-dried.

Images were collected with a Tecnai F20 electron microscope (FEI) on a 4k x 4k CCD detector (Tietz) at a nominal magnification of 50,000 and an underfocus level that placed the first minimum in the contrast transfer function at 18 Å. Images were binned by a factor of two, resulting in a pixel size of 3.47 Å at the specimen level. Low dose settings were used exposing with ~100 $e^-/Å^2$ which significantly improved the signal-to-noise ratio without incurring a loss of structural information to the resolution of the current study.

Single particles analysis

Single molecular views were chosen manually from the micrographs using Boxer, part of EMAN (Ludtke et al., 1999). A total of 8055 images were collected for the CSN-SCF~$N8^{Skp2/Cks1}$ dataset; 4761 for the CSN-SCF~$N8^{Fbw7}$ dataset; 5165 for the $CSN^{Csn5H138A}$ dataset; 4379 for the $CSN^{Csn2\Delta N1\text{-}269}$ dataset and 3106 for the $CSN^{\Delta Csn5}$-SCF~$N8^{Skp2/Cks1}$ dataset. The data stacks were high-pass filtered at 1/250 $Å^{-1}$, masked with a circle and normalized to zero mean and standard deviation of 2 in IMAGIC-5 (van Heel et al., 1996) and low-pass filtered at 1/15 $Å^{-1}$ with the fq command SPIDER (Frank et al., 1996), choosing the Fermi filter option.

Initial classification was performed with the reference-free classification routine refine2d from EMAN. Different sets of three different class averages with high signal-to-noise ratio were selected and submitted to the C1 start up routine in IMAGIC until the program returned near orthogonal Euler angle assignments. A 3D reconstruction from those three class averages was calculated in IMAGIC and the three corresponding re-projections were used as an anchor set for assigning Euler angles to the remaining initial class averages. The calculated 3D model was used as the starting point for refinement.

Refinement consisted of iterated rounds of multi-reference alignment performed in SPIDER, multivariate statistical analysis (MSA) of the newly aligned dataset followed by hierarchical ascendant classification and angular assignment through

projection-matching performed in IMAGIC. The agreement between the appearance of class averages and corresponding structure re-projections was used as a manual selection criterion before calculating the final 3D reconstruction of each refinement round.

Three-Dimensional Reconstructions

Three-Dimensional Reconstructions were calculated using a locally developed program, described in detail below.

In single particle analysis, three-dimensional reconstruction from a set of projection images is typically carried out by weighted back projection. In this process the individual two-dimensional projection images are back projected into the reconstructed three-dimensional volume in directions defined by Euler angles, which have been assigned as part of the analysis. The reconstruction is obtained by summing all of these contributions. A weighting procedure is required to correct for the resulting inherent unequal distribution of contributed data at different spatial frequencies. The exact filter three-dimensional reconstruction procedure of (Harauz and van Heel, 1986) takes account of this effect as well as allowing for any unequal angular distribution of the input data. This is achieved by considering the equivalence between two-dimensional projections of a three-dimensional object in real space and central sections of its three-dimensional Fourier transform (the central section theorem). For a finite object, each such Fourier central section has a depth, which is reciprocally related to the dimension of the reconstructed object in the direction of projection. From these considerations two-dimensional weighting functions in Fourier space can be evaluated which take account of the overlapping contributions from the rest of the data set for each Fourier coefficient of an input image. These weighting (or filter) functions are then used to filter the Fourier transforms of each of the input images which are then transformed back into real space and back projected.

The Fourier space three-dimensional reconstruction used here represents an implementation of the weighting scheme described by (Harauz and van Heel, 1986) but in this case the weighting is applied directly to the three-dimensional Fourier transform of the reconstructed volume. Fourier transforms of each input image undergo a coordinate transformation defined by their assigned Euler angles thereby creating central sections through the three-dimensional transform. Contributions from each coefficient of the Fourier transform of the input images are added to the three-

dimensional Fourier transform using a geometrical weighting function (w_g) derived from the fractional distance between the input Fourier coefficient and the output three-dimensional Fourier coefficient (df) expressed as a fraction of the reciprocal extent of the reconstructed object (do) measured in the direction of the vector between the Fourier coefficients.

$$w_g = \mathrm{sinc}(\pi.(df/do))$$

The three-dimensional Fourier transform of the reconstructed volume is evaluated by summing the weighted contributions of all the input data in a manner similar to the procedure used by FREEALIGN program (Grigorieff, 2007)

$$F_{3D} = (\sum F_{2D} \,.\, w_g) \,/\, (f + \sum w_g)$$

Where F_{3D} is a Fourier coefficient of the three-dimensional Fourier transform of the reconstructed volume, F_{2D} are the Fourier coefficients of the input images and f is a constant (similar to a Weiner filter), typically set to 0.1 of the mean value of w_g, which is included to avoid overrepresentation of sparse data. Additional weighting terms are included to take account of the contrast transfer function (CTF) and to allow effective CTF amplitude correction of data from unstained cryo-electron microscope images. However, these are not relevant to the analysis of negative stained data and are not described here. To increase the accuracy of the procedure the Fourier transforms of both the input images and the three-dimensional reconstruction are subsampled by padding the input images in boxes n x the original dimensions. A typical value for n is 2. Once all the input data have been merged in Fourier space the three-dimensional reconstruction in real space is obtained by Fourier transformation. The program, icrmake3d, is written in C++, reads input images and their Euler angles in Imagic format and outputs a three-dimensional reconstruction in Imagic format.
The resulting three-dimensional reconstructions are characterised by a cleaner background while retaining at least as good a recovery of detail compared to other readily accessible software

Difference Map Analysis

Difference map analysis was performed in IMAGIC. The respective binary masked maps were aligned to each other in three dimensions, normalized to the same standard deviation and subtracted. The resultant difference density was low-pass filtered at

1/25 $Å^{-1}$ and displayed in Chimera at similar contour levels to the corresponding reconstructions. The segmentations shown in Figure S1D were determined via overlays with the corresponding CSN-SCF maps.

Structure visualization and docking of atomic coordinates into EM map

UCSF Chimera (Goddard et al., 2007) and Pymol (www.pymol.org) were used for visualization of EM maps and figure generation. Atomic coordinates of X-ray crystallographic structures and/or EM maps were docked into the electron density of the EM maps in UCSF Chimera using the fit in map function. Agreement between maps and fitted coordinates was quantitatively evaluated within local masks using Uro (Navaza et al., 2002).

Supplemental References

da Fonseca, P.C., He, J., and Morris, E.P. (2012). Molecular model of the human 26S proteasome. Molecular cell *46*, 54-66.

Duda, D.M., Borg, L.A., Scott, D.C., Hunt, H.W., Hammel, M., and Schulman, B.A. (2008). Structural insights into NEDD8 activation of cullin-RING ligases: conformational control of conjugation. Cell *134*, 995-1006.

Duda, D.M., Olszewski, J.L., Tron, A.E., Hammel, M., Lambert, L.J., Waddell, M.B., Mittag, T., DeCaprio, J.A., and Schulman, B.A. (2012). Structure of a Glomulin-RBX1-CUL1 complex: inhibition of a RING E3 ligase through masking of its E2-binding surface. Molecular cell *47*, 371-382.

Enchev, R.I., Schreiber, A., Beuron, F., and Morris, E.P. (2010). Structural insights into the COP9 signalosome and its common architecture with the 26S proteasome lid and eIF3. Structure *18*, 518-527.

Frank, J., Radermacher, M., Penczek, P., Zhu, J., Li, Y., Ladjadj, M., and Leith, A. (1996). SPIDER and WEB: processing and visualization of images in 3D electron microscopy and related fields. J Struct Biol *116*, 190-199.

Goddard, T.D., Huang, C.C., and Ferrin, T.E. (2007). Visualizing density maps with UCSF Chimera. J Struct Biol *157*, 281-287.

Grigorieff, N. (2007). FREALIGN: high-resolution refinement of single particle structures. Journal of structural biology *157*, 117-125.

Gusmaroli, G., Figueroa, P., Serino, G., and Deng, X.W. (2007). Role of the MPN subunits in COP9 signalosome assembly and activity, and their regulatory interaction with Arabidopsis Cullin3-based E3 ligases. Plant Cell *19*, 564-581.

Harauz, G., and van Heel, M. (1986). Exact filters for general geometry three dimensional reconstruction. Optik *73*.

Ludtke, S.J., Baldwin, P.R., and Chiu, W. (1999). EMAN: semiautomated software for high-resolution single-particle reconstructions. J Struct Biol *128*, 82-97.

Navaza, J., Lepault, J., Rey, F.A., Alvarez-Rua, C., and Borge, J. (2002). On the fitting of model electron densities into EM reconstructions: a reciprocal-space formulation. Acta crystallographica Section D, Biological crystallography *58*, 1820-1825.

Pathare, G.R., Nagy, I., Bohn, S., Unverdorben, P., Hubert, A., Korner, R., Nickell, S., Lasker, K., Sali, A., Tamura, T., *et al.* (2012). The proteasomal subunit Rpn6 is a molecular clamp holding the core and regulatory subcomplexes together. Proceedings of the National Academy of Sciences of the United States of America *109*, 149-154.

Roy, A., Kucukural, A., and Zhang, Y. (2010). I-TASSER: a unified platform for automated protein structure and function prediction. Nature protocols *5*, 725-738.

Scott, D.C., Monda, J.K., Bennett, E.J., Harper, J.W., and Schulman, B.A. (2011). N-terminal acetylation acts as an avidity enhancer within an interconnected multiprotein complex. Science *334*, 674-678.

Souphron, J., Waddell, M.B., Paydar, A., Tokgoz-Gromley, Z., Roussel, M.F., and Schulman, B.A. (2008). Structural dissection of a gating mechanism preventing misactivation of ubiquitin by NEDD8's E1. Biochemistry *47*, 8961-8969.

van Heel, M., Harauz, G., Orlova, E.V., Schmidt, R., and Schatz, M. (1996). A new generation of the IMAGIC image processing system. J Struct Biol *116*, 17-24.

Zheng, N., Schulman, B.A., Song, L., Miller, J.J., Jeffrey, P.D., Wang, P., Chu, C., Koepp, D.M., Elledge, S.J., Pagano, M., *et al.* (2002). Structure of the Cul1-Rbx1-Skp1-F boxSkp2 SCF ubiquitin ligase complex. Nature *416*, 703-709.

Supplemental Figures and Text

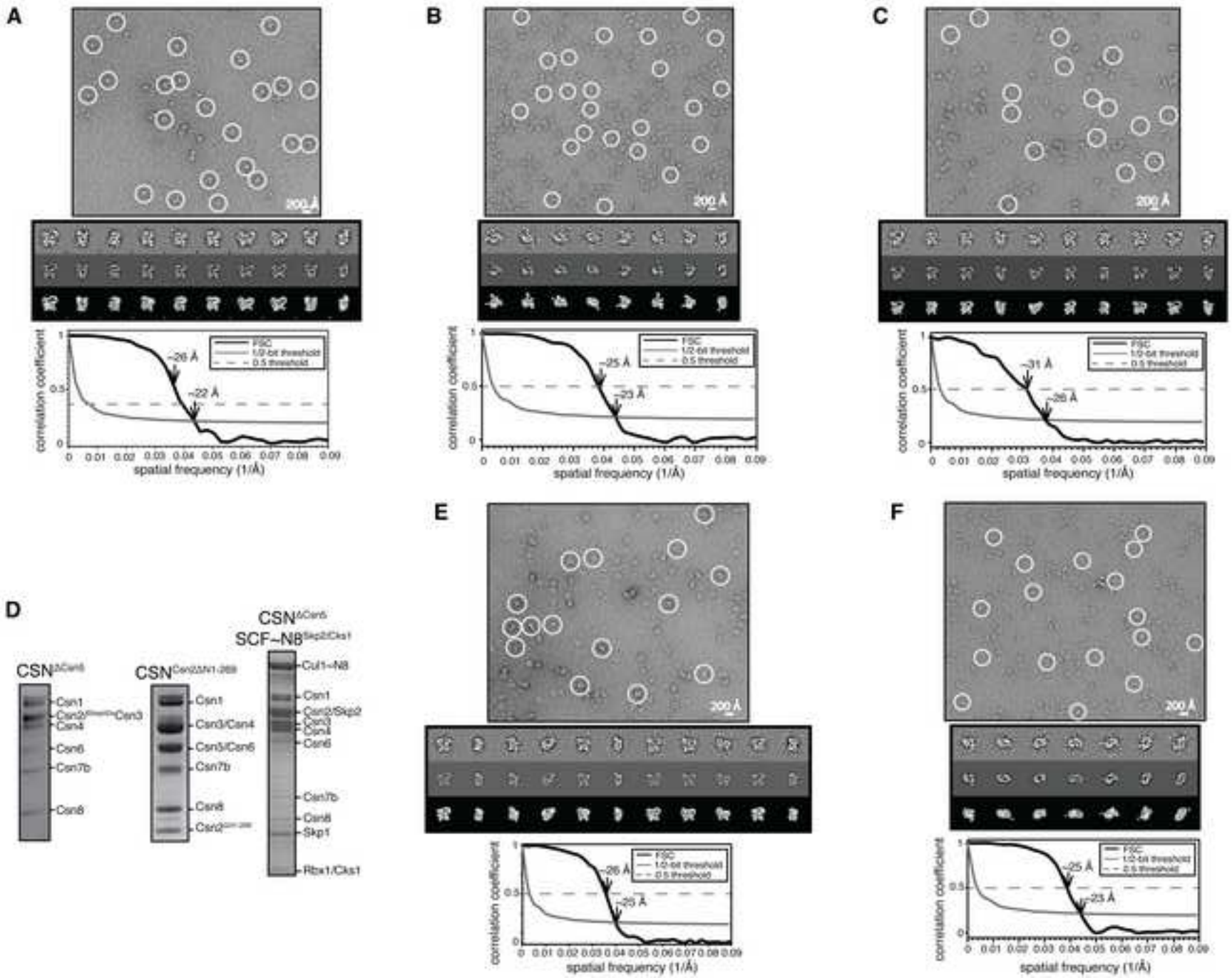

Supplemental Figures and Text

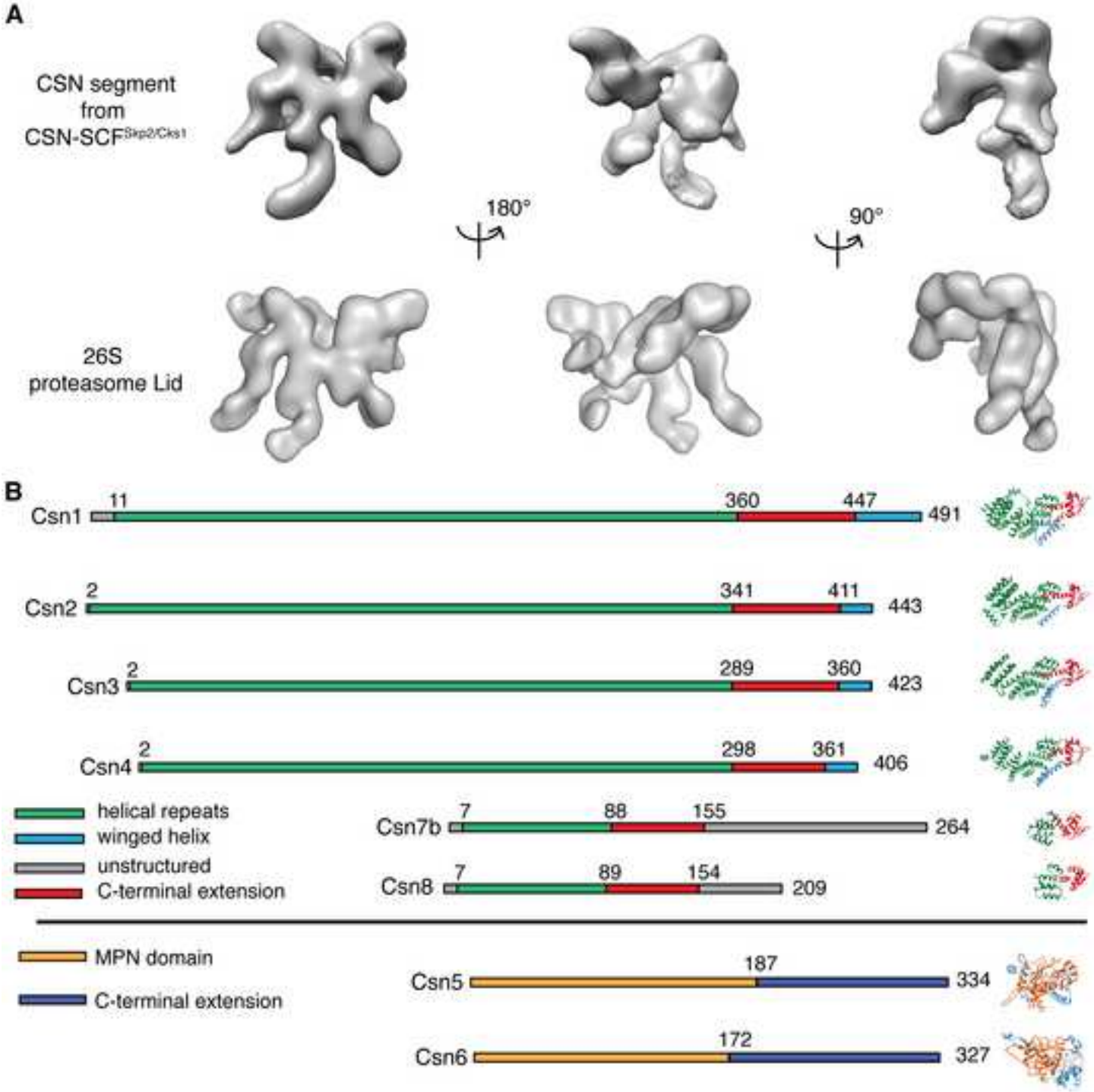

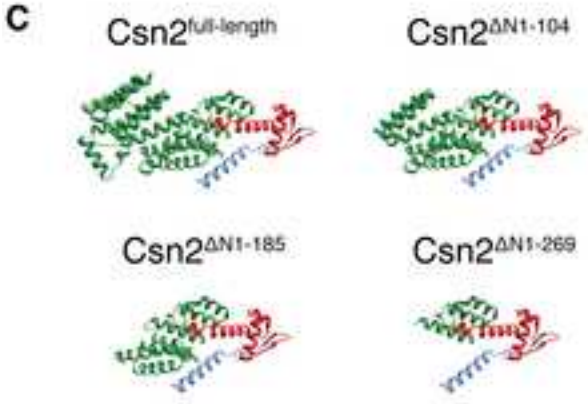

D

subunit	correlation coefficient
Csn1	0.76
Csn2	0.85
Csn3	0.82
Csn4	0.79
Csn5	0.93
Csn6	0.87
Csn7	0.98
Csn8	0.98
Cul1	0.93
Skp1	0.98
Skp2	0.98
Cks1	0.99

Supplemental Figures and Text

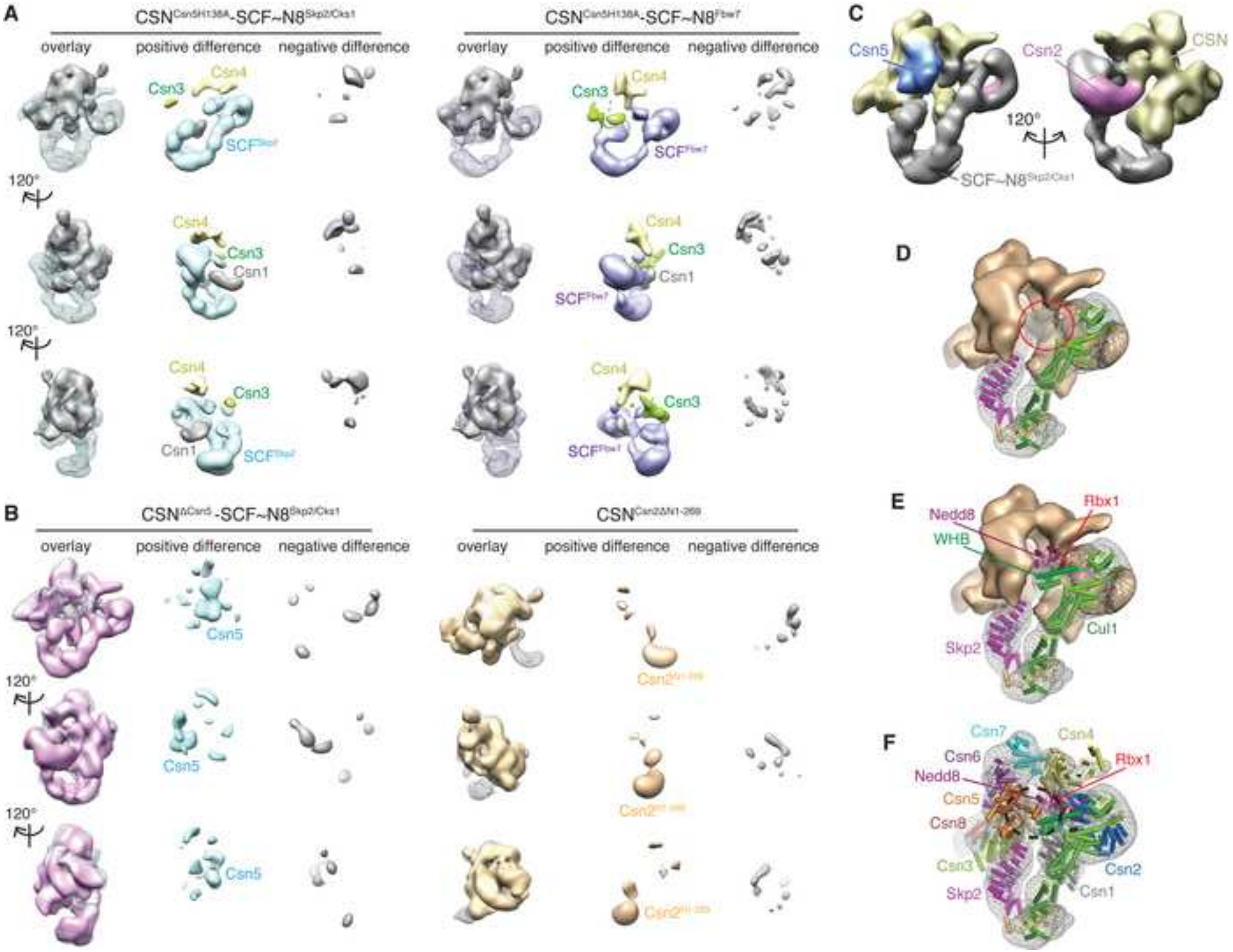

Supplemental Figures and Text

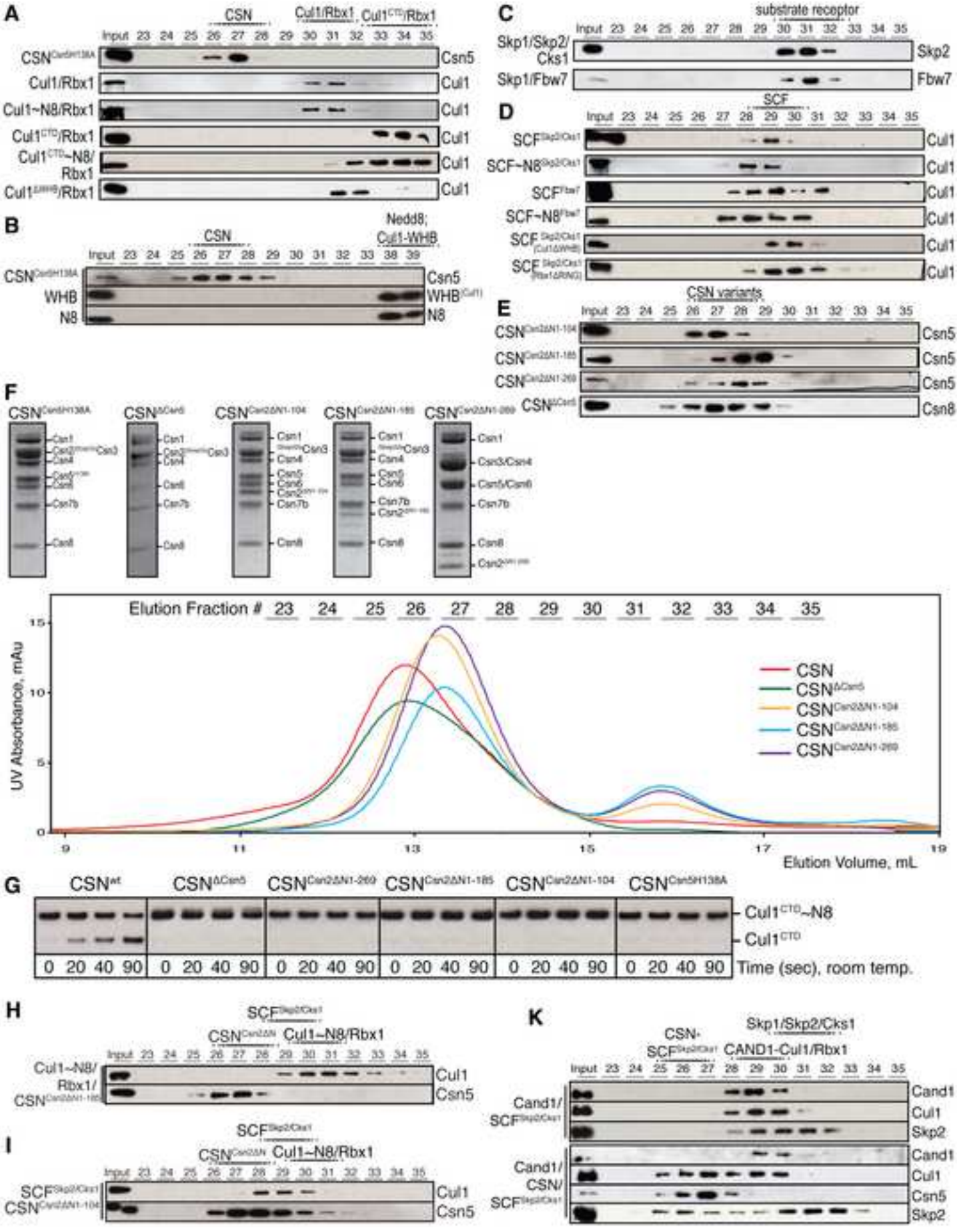

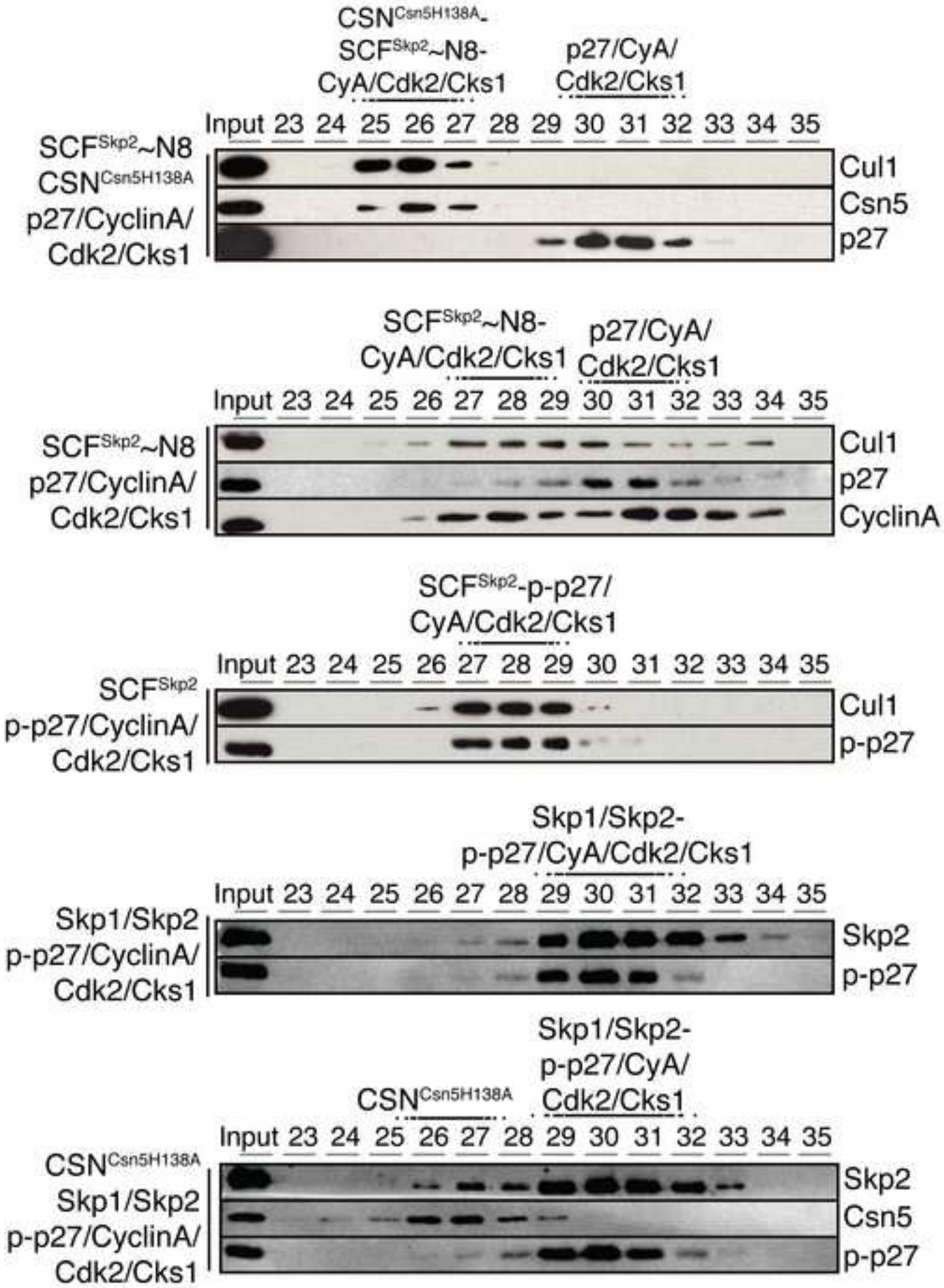
CSN^Csn5H138A-
SCF^Skp2~N8-
CyA/Cdk2/Cks1
p27/CyA/
Cdk2/Cks1
Input 23 24 25 26 27 28 29 30 31 32 33 34 35
SCF^Skp2~N8
CSN^Csn5H138A
p27/CyclinA/
Cdk2/Cks1
Cul1
Csn5
p27
SCF^Skp2~N8-
CyA/Cdk2/Cks1
p27/CyA/
Cdk2/Cks1
Input 23 24 25 26 27 28 29 30 31 32 33 34 35
SCF^Skp2~N8
p27/CyclinA/
Cdk2/Cks1
Cul1
p27
CyclinA
SCF^Skp2-p-p27/
CyA/Cdk2/Cks1
Input 23 24 25 26 27 28 29 30 31 32 33 34 35
SCF^Skp2
p-p27/CyclinA/
Cdk2/Cks1
Cul1
p-p27
Skp1/Skp2-
p-p27/CyA/Cdk2/Cks1
Input 23 24 25 26 27 28 29 30 31 32 33 34 35
Skp1/Skp2
p-p27/CyclinA/
Cdk2/Cks1
Skp2
p-p27
Skp1/Skp2-
p-p27/CyA/
Cdk2/Cks1
CSN^Csn5H138A
Input 23 24 25 26 27 28 29 30 31 32 33 34 35
CSN^Csn5H138A
Skp1/Skp2
p-p27/CyclinA/
Cdk2/Cks1
Skp2
Csn5
p-p27

Supplemental Figures and Text

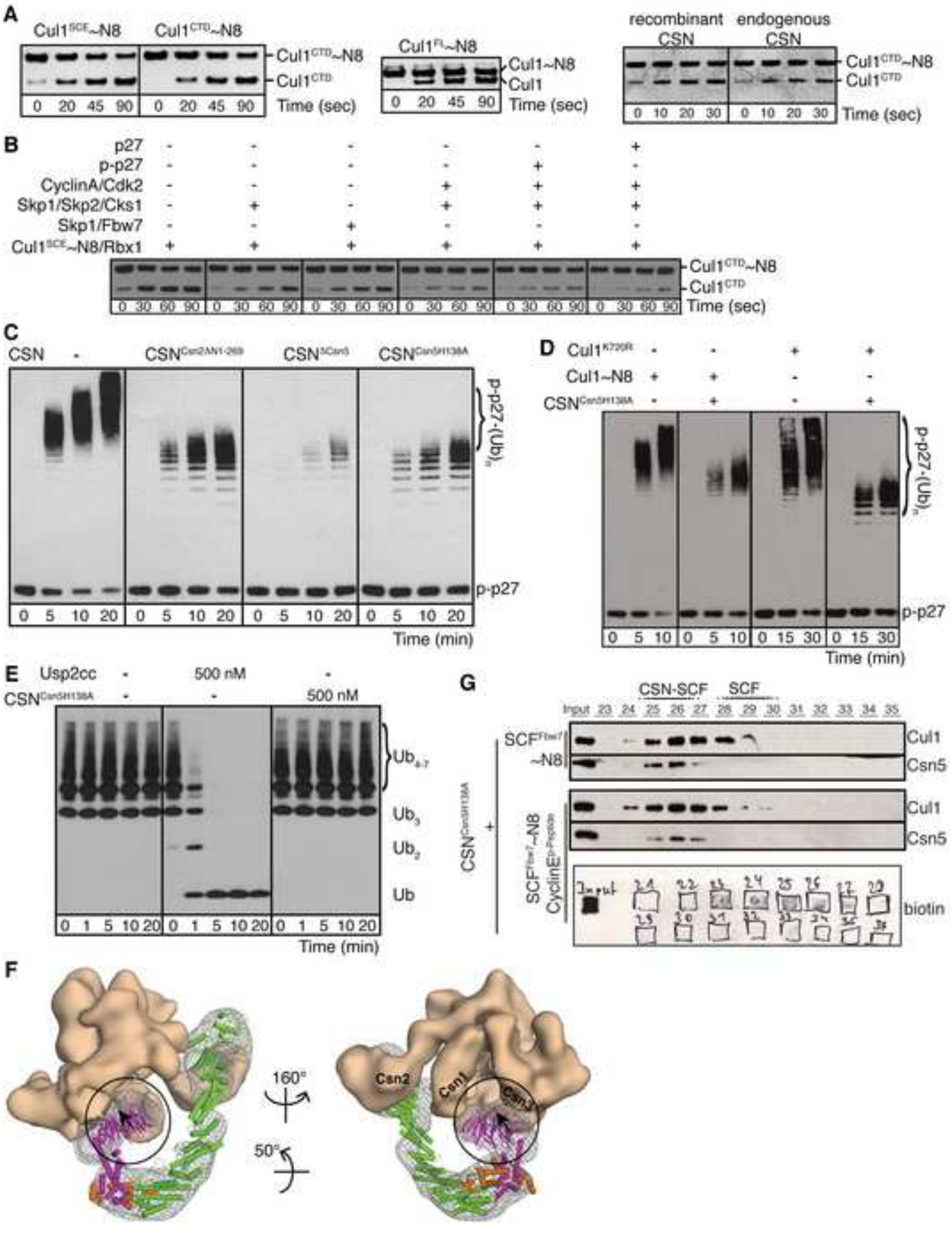

Supplemental Figures and Text